Materials Today Bio 18 (2023) 100552

Contents lists available at ScienceDirect

Materials Today Bio

journal homepage: www.journals.elsevier.com/materials-today-bio

The CuO and AgO co-modified ZnO nanocomposites for promoting wound healing in *Staphylococcus aureus* infection☆

Lisong Ye [a,1], Xiaojun He [b,1], Enoch Obeng [b], Danyan Wang [c], Dongyang Zheng [a], Tianxi Shen [a], Jianliang Shen [b,c,***], Rongdang Hu [a,**], Hui Deng [a,*]

[a] School of Stomatology, Wenzhou Medical University, Wenzhou, Zhejiang, 325035, China
[b] School of Ophthalmology & Optometry, School of Biomedical Engineering, Wenzhou Medical University, Wenzhou, Zhejiang, 325035, China
[c] Wenzhou Institute, University of Chinese Academy of Sciences, Wenzhou, 325000, China

ARTICLE INFO

Keywords:
CuO@AgO/ZnO NPs
Photothermal therapy
Antibacterial
Anti-biofilm
Wound healing

ABSTRACT

Bacterial has become a common pathogen of humans owing to their drug-resistant effects and evasion of the host immune system, with their ability to form biofilm and induce severe infections, a condition which has become a primary public health concern globally. Herein, we report on CuO@AgO/ZnO NPs antibacterial activity enhanced by near-infrared (NIR) light which was effective in the elimination of *Staphylococcus aureus* and the *Pseudomonas aeruginosa*. The CuO@AgO/ZnO NPs under NIR significantly eradicated *S. aureus* and its biofilm and *P. aeruginosa in vitro*, and subsequently exhibited such phenomenon *in vivo*, eliminating bacteria and healing wound. This demonstrated the combined intrinsic antibacterial potency of the Cu and Ag components of the CuO@AgO/ZnO NPs was enhanced tremendously to achieve such outcomes in *vitro* and *in vivo*. Considering the above advantages and facile preparation methods, the CuO@AgO/ZnO NPs synthesized in this work may prove as an important antibacterial agent in bacterial-related infection therapeutics and for biomedical-related purposes.

1. Introduction

As one of the leading causes of global mortality, bacterial infections have become a great public concern. The bacterial resistance to traditional antibiotics and the difficulties accompanying the treatment of the infections-associated disease had contributed immensely to the cost of treatment, with billions of monies being spent every year around the world [1–3]. The bacteria resistance tends to even intensify when it assumes proliferation and complex communication processes to develop into a biofilm. This has largely contributed to surgical and implant failure [4,5]. Reports have attributed the resistance to uncontrolled and misuse of antibiotics in an attempt to strictly treat infection-related conditions, in the long round compounding the problem and greatly increasing the financial burden for treatment [6,7]. Hence, it's paramount to develop an alternative means to replace traditional antibiotics.

In recent years one of the few anti-infective therapies which have gained recognition for their economical and effective means of eradicating bacteria is photothermal therapy (PTT). The therapy employs photothermal agents (PTAs) to effectively undertake therapeutic tasks [8–10]. These PTAs directly absorb and convert light energy from a laser to heat (localized hyperthermia) to effectively kill pathogenic organisms. Also, the PTT allows for deep penetration of its target, hence suitable and yet could be harmful when singly employed. Reports indicate that too much ultraviolet light will be harmful to the human body, such as cancer, whereas near-infrared light is completely harmless [11–13]. Considering its advantages and controllability, PTT has a great prospect of being used as part of the alternative process for tackling antibiotic resistance and bacterial-related infections. In addition, Nanotechnology has presented nanoparticles (NPs) as PTAs, this includes metal nanoparticles, conjugate polymers, metal sulfides, etc. That can be grouped into either organic or inorganic NPs [14–16]. A critical examination of both groupings brings out their peculiar properties, which account for the outstanding and

☆ All authors have approved the final version of this manuscript.

* Corresponding author.
** Corresponding author.
*** Corresponding author. School of Ophthalmology & Optometry, School of Biomedical Engineering, Wenzhou Medical University, Wenzhou, Zhejiang, 325035, China.
E-mail addresses: shenjl@wiucas.ac.cn (J. Shen), hurongdang@hotmail.com (R. Hu), dh0726@163.com (H. Deng).

[1] These authors contributed equally to this work.

https://doi.org/10.1016/j.mtbio.2023.100552
Received 25 October 2022; Received in revised form 12 December 2022; Accepted 26 December 2022
Available online 14 January 2023

tremendous function of each grouping. These inorganic or organic NPs could be singly employed or combined as nanocomposites to achieve a synergistic antimicrobial function. Compared with organic antimicrobial agents, inorganic antimicrobial agents such as Au NPs, Ti NPs, etc. Have received more attention for their low toxicity, environmental friendliness, and good stability against various bacteria [17–19]. On the one hand, Zinc Oxide (ZnO) NPs are multifunctional inorganic material that has widely been used for their favorable properties in biomedicine [20], sensor [21], energy conversion [22], catalysis [23], and optical fields [24], etc. In the field of biomedicine, it has been demonstrated that ZnO NPs are useful at accelerating wound healing [25,26].

However, the photothermal efficiency and the antibacterial properties of ZnO NPs are reported to be relatively low [27,28]. Particularly, a study shows ZnO NPs' antimicrobial activity was greatly enhanced after their modification with other metal compounds [29]. Silver (Ag) NPs on the other hand have greatly been used to modify ZnO NPs, due to their intrinsic antibacterial property and catalytic activity [30–32]. Studies indicate the release of Ag ions are able to bind with enzymes thiol groups of bacteria to sequentially trigger cell death [33–35]. Furthermore, among the inorganic NPs is the Cu-based NPs, an essential trace element that has gained much attention owing to its essential properties. Like other noble metals, Cu NPs demonstrates electric and thermal conductivity and have varying synthesis process. Cu NPs have been employed in tumor, rheumatoid arthritis, antibacterial and other related treatments [36,37]. Next, the Cu-based NPs requires mild synthesis process, they have low toxicity and good biocompatibility. Copper oxide (CuO) NPs was employed for their PTT properties, stable performance, angiogenesis and bone cartilage formation effect [38,39]. For synergistical purposes nanocomposites have been widely studied and gain attention as mentioned earlier [40]. Hence developing of a nanocomposite with PTT functionality will hold the possibility of significantly dealing with the aforementioned menace.

Herein, we report on CuO and AgO co doped ZnO nanocomposites prepared via the classic sol gel method, calcined at 600 °C to give an impurity free CuO@AgO/ZnO NPs. CuO@AgO/ZnO NPs demonstrated good photothermal stability, intrinsic antibacterial activity and synergistically enhanced antibacterial efficiency under NIR. CuO@AgO/ZnO NPs under NIR effectively killed both the *Staphylococcus aureus* and *Pseudomonas aeruginosa in vitro*. Also, under the CuO@AgO/ZnO NPs therapeutic nanocomposite, the rapid healing of *S. aureus* infected wounds and the tremendous recovery of tissues with negligible inflammatory effect were demonstrated *in vivo* (Scheme 1). Finally, CuO@AgO/ZnO NPs displayed good hemocompatibility and biocompatibility demonstrating their prospect for treatment of bacterial infections, wound healing and biomedically related application.

2. Experimental section

2.1. Materials

Zinc acetate (Zn $(Ac)_2$), sodium hydroxide (NaOH), copper sulfate ($CuSO_4$), silver nitrate ($AgNO_3$), and hydrochloric acid (HCl, 37%) with >99.0 purity were obtained from Sigma-Aldrich. Polyethylene glycol (PEG, Wt = 400), hydrazine hydrate (N_2H_4 H_2O, 50%), L-ascorbic acid (AA), and Ethanol were obtained from Nanjing Reagent. Working solutions were used as obtained, and deionized water was used in dilutions and other preparations.

2.2. Synthesis of ZnO and CuO@AgO/ZnO NPs

As reported by Cao and Nie et al. [41,42], $Zn(Ac)_2$ and NaOH were firstly dissolved in equal parts to give 60 mL of 0.1 mol L^{-1} Zn $(Ac)_2$ solution and 60 mL of 0.5 mol L^{-1} NaOH solution. The solutions were thoroughly mixed using a magnetic stirrer for 6 h. The pH was carefully adjusted between 10 and 11 during the mixing and stirring process. The solution was then transferred to a 180 mL autoclave and kept in an oven at 185 °C for 12 h, to obtain the ZnO nanocrystals. The obtained white precipitate was washed alternately with deionized water and 100% ethanol. The step was repeated five times and the product was repeatedly redispersed and filtered. The product was desiccated at 70 °C for 8 h. This was followed by calcination at 600 °C for 5 h to give the ZnO NPs. Using the same procedure, CuO and AgO were successfully fabricated. Next, with a mole ratio of 0.05 for ZnO, CuO, and AgO respectively, their resulting nanopowders were redispersed in deionized water and stirred

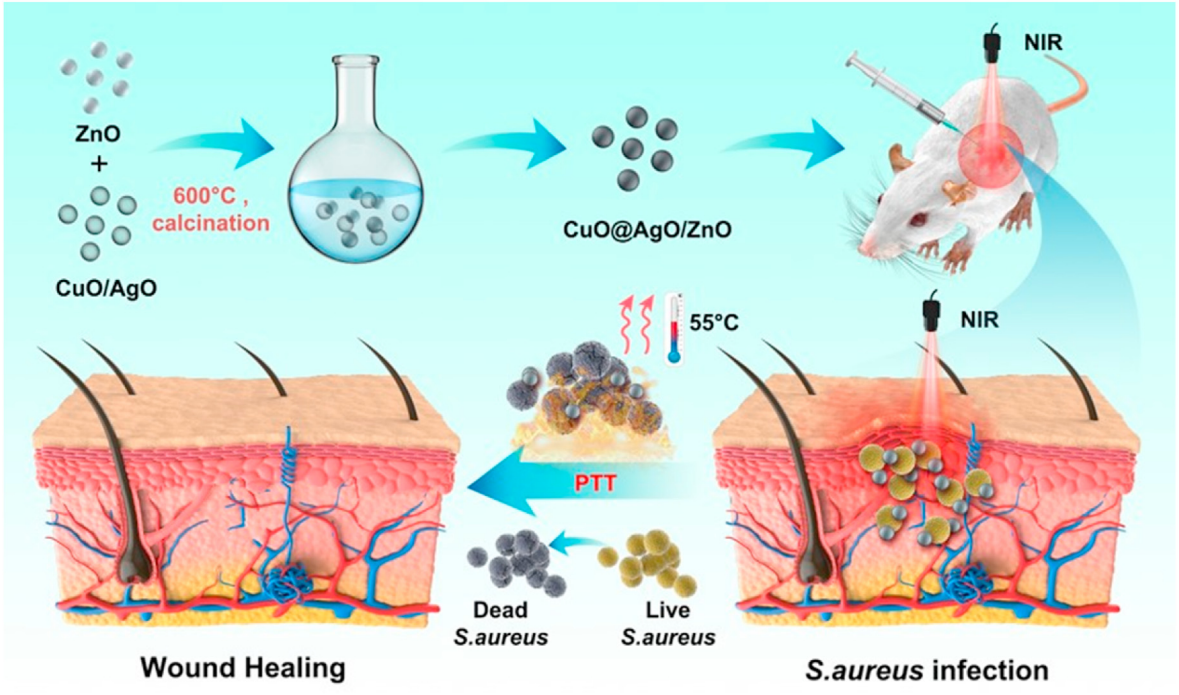

Scheme 1. Schematic illustration of CuO@AgO/ZnO NPs fabrication and the antibacterial effect in a wound-infection model *in vivo*.

on a magnetic stirrer continually for 4 h. The product (CuO@AgO/ZnO) obtained was once again dried and calcinated as done earlier (600 °C, 5 h) and the resulting product (CuO@AgO/ZnO NPs) was characterized.

2.3. Characterization of ZnO and CuO@AgO/ZnO NPs

Using Technai G2 F20 microscope for the Transmission electron microscopy images and High-resolution transmission electron microscopy (HRTEM), D/MAX 2005 Rigaku X-ray diffractometer for the X-ray diffraction patterns (XRD), Thermo Fisher X-ray photoelectron spectrophotometer K-alpha for X-ray Photoelectron Spectroscopy (XPS) and CARY 5000 spectrophotometer for the UV–vis Spectroscopy the structure and morphology of ZnO and CuO@AgO/ZnO NPs were characterized. CuO@AgO/ZnO NPs were labeled as CAZ.

2.4. In vitro cytotoxicity study

Before conducting the antibacterial and animal experiments, the biosafety of CAZ was first tested using L929 fibroblasts. 100 μL aliquots of different concentrations of CAZ solutions were added to 96-well plates in which L929 cells in the logarithmic growth phase existed. The control group was treated with PBS and after exposed to NIR (808 nm, 2 W cm^{-2}, 7 min). After 48 h, an equal amount of MTT solvent was applied to each well and mixed well. The absorbance of each well was measured with a microplate reader after 4 h. The cell viability of the control group was designated as 100% for the final data analysis.

2.5. In vitro antibacterial tests

The antibacterial performance of CAZ was evaluated using *S. aureus* and *P. aeruginosa* as model strains. For the *in vitro* antibacterial experiments, 100 μL of *S. aureus* and *P. aeruginosa*-diluted liquid broths were separately added to each well of a 96-well plate, followed by treatment with, 100 μL of PBS, ZnO, and CAZ solution (200 μg mL^{-1}). After thorough mixing, the sample was placed in a bacterial incubator at 37 °C for 2 h, and then irradiated with NIR light (808 nm, 2 W cm^{-2}, 7 min). After a 4 h additional incubation at 37 °C, the mixture was diluted (1:400) with sterile PBS and 25 μL of each diluted sample was spread on the surface of a tryptic soy agar plate. After 16 h of incubation at 37 °C, multiple counts of *S. aureus* and *P. aeruginosa* colonies formed on the surface of the plates were quantified, and the results were used to evaluate the antibacterial performance. In addition, a live/dead staining assay was performed, and PBS, ZnO, and CAZ-treated bacteria were stained by adding the appropriate amount of LIVE/DEAD BacLight reagent, and later observed with the confocal fluorescence microscopy imaging system.

2.6. Biofilm assay of S. aureus

Under the *in vitro* biofilm assay, 200 μL of PBS, ZnO, CAZ treated bacteria and treatments exposed to NIR irradiation were first transferred to a six-well plate, and then an equal amount of 3 mL of fresh trypsin soy broth was added to each well. Quantitative measurements were performed with crystal violet staining after 48 h incubation under 37 °C of bacterial culture. Specifically, the six-well plate was washed three times with PBS to wash off planktonic bacteria that did not form a biofilm. 0.2% crystal violet was added for 20 min staining and the excess crystal violet was washed off with PBS. Finally, 33.3% acetic acid was added to dissolve the crystal violet in the biofilm, and the biofilm content was evaluated by measuring the absorbance with a microplate reader at a wavelength of 595 nm [43]. Biofilms were later stained with mixed calcein-AM/PI dyes living/dead cell double staining kit (HRO444) in the dark for 15 min and afterward, visualized with a fluorescence confocal microscope (Nikon Eclipse Ti A1, Japan). Three parallel groups were set for each condition group.

2.7. Hemolysis assay of S. aureus

The hemolytic activity of *S. aureus* was performed by centrifuging the suspensions of bacteria treated differently with PBS, ZnO, and CAZ at 5000 rpm for 10 min, and the supernatants were collected. Meanwhile, fresh rabbit erythrocytes were washed 3 times with PBS to remove damaged erythrocytes. 0.5 mL of bacterial supernatant and 0.5 mL of rabbit erythrocyte solution were mixed and left to stand for 1 h at 37 °C. Final centrifugation at 5000 rpm for 10 min was performed to collect the supernatant of each group of mixtures. The supernatant's hemoglobin content was analyzed by measuring the absorbance at a wavelength of 595 nm with a microplate reader, to reflect the hemolytic activity of each group. Three parallel groups were set for each condition group.

2.8. Bacterial morphology study

The morphology of bacteria treated with PBS, ZnO, and CAZ under 808 nm NIR irradiation was evaluated by using scanning electron microscopy. 100 μL of separately treated *S. aureus* and *P. aeruginosa* solutions were added to 900 μL of 2.5% glutaraldehyde solution, fixed at 4 °C for 12 h and after being treated with different gradients of ethanol solutions (50%, 70%, 80%, 90%, 95%, & 100%) for dehydration, each step was carried out for 10 min 5 μL of the bacterial solution was then dropped onto the silicon wafer. The silicon wafers were dried in an oven at 60 °C for 12 h and then coated with ultrathin gold by sputtering and further imaged using a Hitachi Su 8010 instrument at 3.0 kV.

2.9. Bactericidal effect in vivo

All animal experiments were performed in accordance with the stated guidelines of the Animal Ethics Committee of Wenzhou Medical University (SYXK-2021-0020).

The *In vivo* antibacterial assay was investigated by establishing a local wound healing model using BALB/c mice. Firstly, the hair on the back of the mice was removed with a razor and a depilatory cream, and the area was disinfected. A hole puncher was then used to create a small equal-sized prototype wound on the back of the mice. Next, a suspension of *S. aureus* (10 μL, $OD_{600} = 0.5$) was evenly spread on the mouse wound to cause wound infection. And then 20 μL of PBS, ZnO, and CAZ suspension were injected into the wound site and further exposed to 808 nm NIR irradiation. An infrared thermal imager was used to observe and record the skin temperature changes near the wounds of the mice. A digital photograph of the wound site was taken every two days. Image J software was used to analyze the digital photos to calculate the change in wound area in BALB/c mice. The bacterial content in the wounds of mice in different groups was quantified by the standard plate count method to evaluate the bacteria effect *in vivo*. Histological analysis of skin sections was performed using hematoxylin-eosin staining, Gram staining, and Masson staining to determine the *in vivo* antimicrobial treatment effect of CAZ under NIR. Also, the main organs (heart, liver, spleen, lung, and kidney) of the mice in all the groups were acquired for HE staining and their blood samples were collected for biochemical analysis. Three parallel groups were set for each condition group.

2.10. Photothermal effect of CAZ

The evaluation of the photothermal efficiency was performed by irradiating, 100 μL of CAZ solution with 808 nm NIR light at room temperature. At the same time, the temperature change of the solution was detected with an infrared imager to obtain the heating-cooling curve of CAZ. The photothermal conversion efficiency (η) was calculated by the following formula:

$$\eta = \frac{\mathrm{hS}\left(T_{max,\mathrm{CAZ}} - T_s\right) - Q_0}{\mathrm{I}\left(1 - 10^{-A808}\right)} \quad (1)$$

$$\tau_s = \frac{m_d C_d}{hS} \tag{2}$$

$$Q_0 = \mathrm{hS}\ (T_{max,water} - T_s) \tag{3}$$

The value of τ_s, the characteristic thermal time constant, can be determined by using the linear regression curve in the cooling curve. The mass and heat capacity of the solutions were represented by m_d and C_d, respectively. Consequently, the value of hS could be derived from the calculation. In Equation (3), $T_{max,\ water,}$ and Ts represented the stable maximum temperature of water and room temperature, respectively. The Q_0, which can be calculated from Equation (3), represents the background energy input without CAZ. $T_{max,\ CAZ}$ represents the steady-state maximum temperature of the CAZ solution under the experimental conditions, I represent the near-infrared laser power, and A_{808} represents the absorbance of CAZ at 808 nm NIR. Finally, the above data were substituted into Equation (1) to calculate the photothermal conversion efficiency of CAZ.

2.11. Statistical analysis

All experimental data including cytotoxicity, *in vitro* antibacterial, *anti*-biofilm, hemolysin inhibition, and *in vivo* antibacterial were expressed in the mean ± standard deviation (SD). The statistical data were analyzed by a student's t-test. The difference was statistically significant when $p < 0.01$, and $p < 0.001$, which were highly significant. Data analysis and graph plotting were done using GraphPad Prism Software 9.3 (USA).

3. Results and discussion

3.1. Synthesis and characterization of ZnO and CAZ

Nanoparticles were successfully synthesized and the structural morphology was characterized. As displayed in the TEM images ZnO could clearly be distinguished from the CuO/AgO/ZnO (Fig. 1a and b). Accordingly, the size range of the ZnO was 81.63 nm–128.92 nm with an average size of 105.85 nm, and that of CuO/AgO/ZnO was 59.77 nm–110.44 nm having an average size of 85.03 nm (Fig. 1c). These results showed the well dispersion of Cu, Ag, and Zn in the CuO/AgO/ZnO

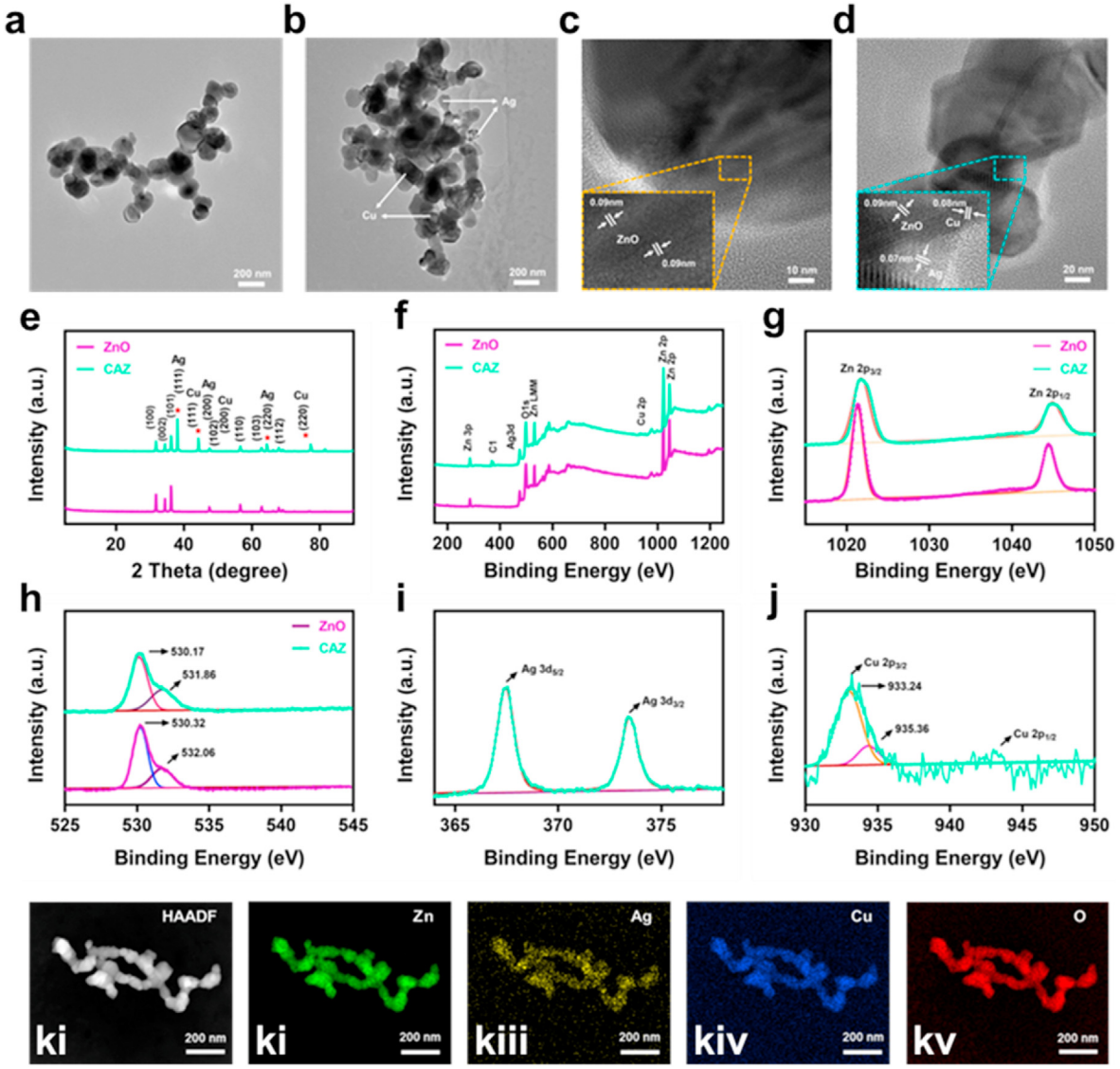

Fig. 1. Characterization of ZnO and CAZ NPs. (a–b) TEM images, (c–d) HRTEM images, (e) XRD patterns, (f) the XPS survey spectrum of ZnO and CAZ NPs, (g) XPS spectra of Zn 2p region, (h) O1s region, (i) Ag 3 d region. (j) And Cu 2p region. (ki-kv) Elemental mapping of the CAZ NPs (scale bar: 200 nm).

nanocomposite. The HRTEM revealed an interplanar spacing of lattice size estimated at 0.090 nm, 0.088 nm, and 0.070 nm for the ZnO, CuO, and AgO respectively (Fig. 1d). Further evaluation of the crystallinity and purity of ZnO and CuO/AgO/ZnO was accomplished via XRD analysis. As shown in (Fig. 1e) the XRD pattern of ZnO marched the hexagonal wurtzite structure (JCPDS card no. 36–1451) with peaks position of (100), (002), (101), (102), (110), (103) (112), (201) and (202) appearing at 31.76º, 34.42º, 36.22º, 47.50º, 56.57º, 62.90º, 67.94º, 69.14º and 77.31º. The presence of Cu and Ag unveiled different peaks (111) (200) (220) marked with (red *) at 44.4º2, 50.53º and 74.06º in the Cu and 38.10º,44.28º,64.44º in the Ag. Although some peaks of Cu were not much visible which could be attributed to the intensity and strength of the other elements. However, the presence of known peaks shows the absence of impurity. As shown in (Fig. 1f), the chemical composition was further analyzed with XPS. The XPS spectrum revealed signals and peaks of 1021.26 eV and 1044.42 eV for Zn2p in the ZnO, 1021.72eV and 1044.89 eV for Zn2p in the CuO/AgO/ZnO (Fig. 1g). The binding energy peaks of O1s in the ZnO were 530.32 eV and 532.06 eV, and that of CuO/AgO/ZnO was estimated at 530.17 eV and 531.86 eV (Fig. 1h). In addition, $3d_{5/2}$ and $3d_{3/2}$ of the Ag were 367.47 eV and 373.47 eV respectively, and that of Cu 2p was 933.24 eV (Fig. 1i and j) which were all in tandem with previous reports, the display of element C by the XPS

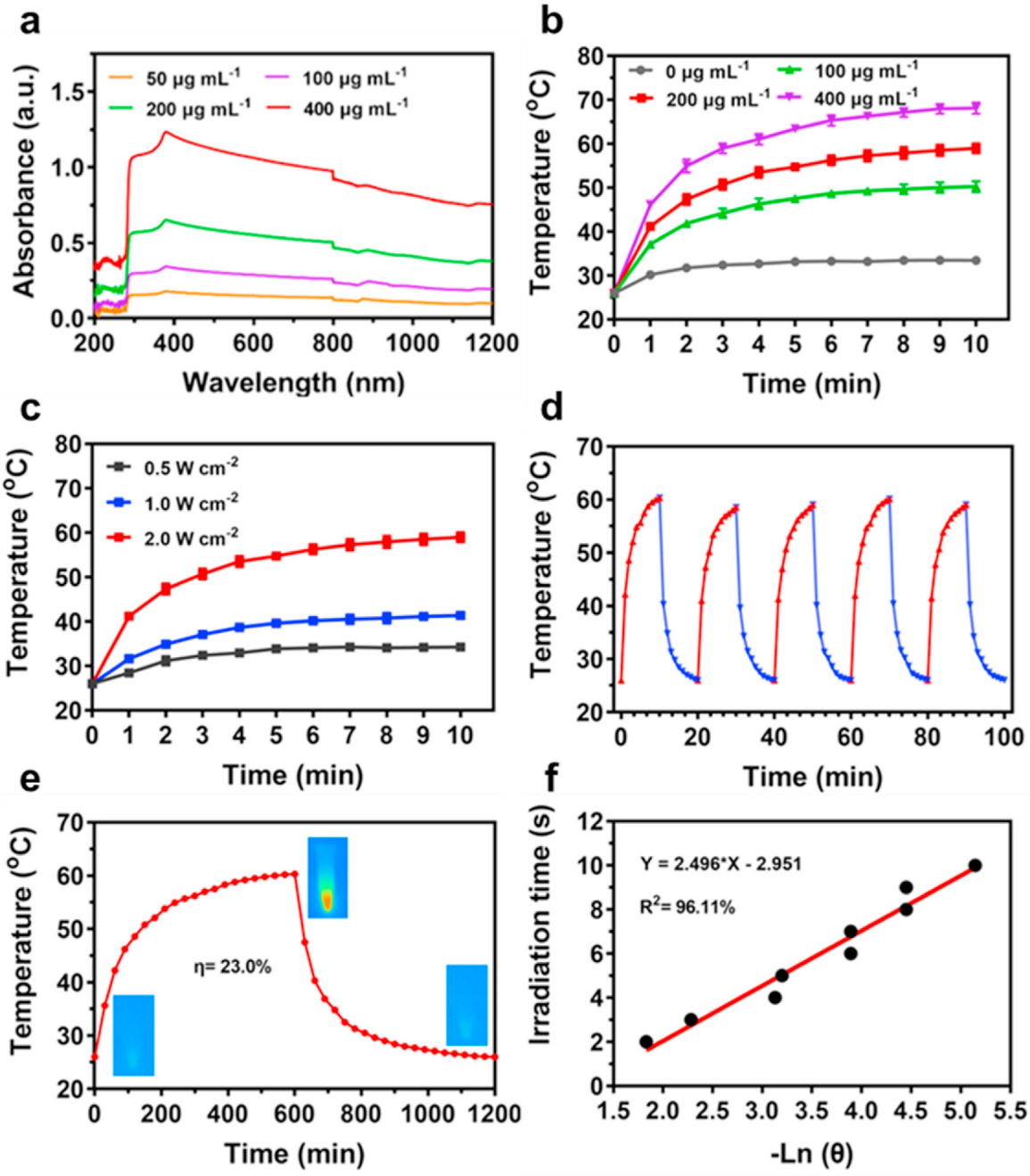

Fig. 2. Photothermal performance and conversion efficiency of CAZ NPs. (a) UV–vis–NIR absorption spectra of CAZ NPs dispersions with different concentrations. (b) Temperature curves of 200 μL CAZ NPs dispersions with different concentrations after 10 min of irradiation (808 nm, 2.0 W cm^{-2}). (c) Temperature variation curves of CAZ NPs dispersion (200 μg mL^{-1}, 200 μL) under different powers densities of 808 nm NIR. (d) The heating and cooling curves of CAZ NPs under five on/off NIR laser cycles (200 μg mL^{-1}, 2.0 W cm^{-2}). (e) The rise and cooling down of the temperature level of CAZ NPs. (f) Linear fitting plots of time versus −ln θ during the cooling period.

spectrum could be attributed to the XPS device [44–47]. Furthermore, images of the elemental mapping confirmed the presence of Zn and O in the ZnO NPs and Zn, Cu, Ag, and O in the CuO@AgO/ZnO nanocomposites (Fig. 1 ki-kv). All these results demonstrate the successful synthesis of the ZnO and CuO@AgO/ZnO with the absence of impurity.

3.2. Photothermal performance of CAZ

A crucial phenomenon expected of a good photothermal agent is the state of absorption and conversing efficiency [48]. Remarkably, CAZ displayed a strong and wide range of absorbance in the near-infrared region, that positively correlated with its concentration (Fig. 2a). The photothermal performance was evaluated based on the exposure of a series of CAZ concentrations (50, 100, 200, 400 μg mL^{-1}) to NIR irradiation (808 nm, 2 W cm^{-2}) for 10 min (Fig. 2b). The temperature of concentration 200 μg mL^{-1} rose rapidly to 55 °C within a time point of about 7 min. Next exposure of the 200 μg mL^{-1} to varying NIR irradiation of different power densities showed that CAZ temperature rise was dependent on the power density and irradiation time (Fig. 2c). This demonstrated that CAZ exhibited a photothermal effect which is greatly influenced by its concentration, power density of laser, and laser irradiation time. Also, to evaluate the photothermal stability, CAZ suspension

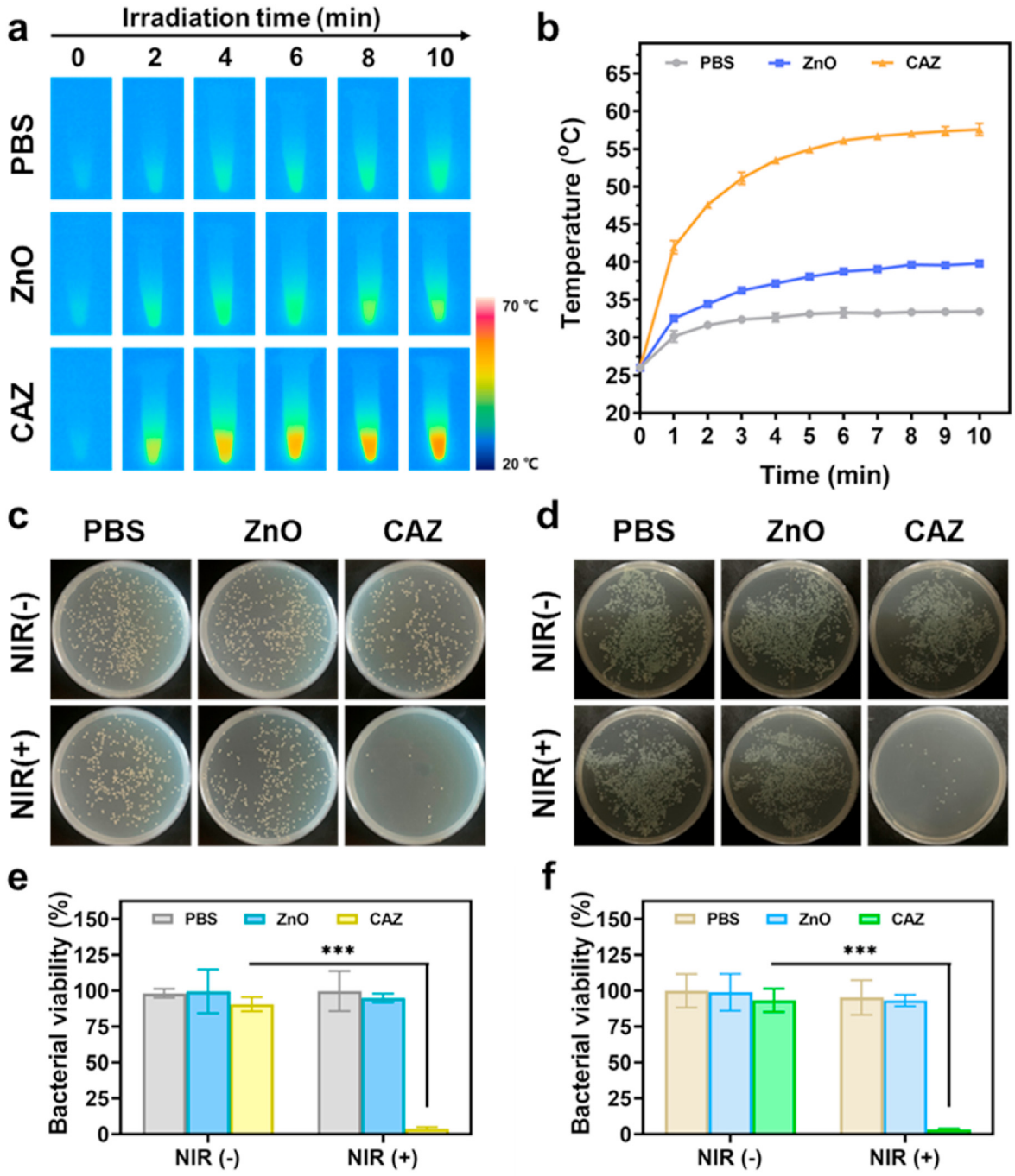

Fig. 3. *In vitro* antibacterial activity of CAZ NPs. (a) Infrared thermal images of PBS, ZnO, and CAZ NPs under 808 nm NIR irradiation (2.0 W cm^{-2}). (b)Temperature changes of *S. aureus* solution during treatment with PBS, ZnO, and CAZ NPs under 808 nm NIR irradiation. Photographic images of bacterial colonies of (c) *S. aureus* and (d) *P. aeruginosa* under different treatments. Bacterial viability of (e) *S. aureus* and (f) *P. aeruginosa* under different treatment conditions. ***$p < 0.001$.

was exposed to NIR (808 nm, 2 W cm^{-2}, 10 min) and under 5 on/off laser cycles CAZ showed significantly stable performance without any remarkable changes (Fig. 2d). Surprisingly the photothermal conversion efficiency (PCE) displayed by the on/off laser curve was 23.0% (Fig. 2e and f), which was higher than other traditional nanoparticles such as Au, Pt, etc. [49–51], a demonstration of CAZ's ability to withstand heat over a prolonged period and possession of high photothermal stability. These results suggested that CAZ could be employed as an effective PTA to generate heat from NIR.

3.3. In vitro antibacterial activity of CAZ

Motivated by CAZ photothermal performance, we evaluated the antibacterial activity *in vitro* using the standard plate count method. The bacteria strains employed were *S. aureus* (Gram-positive) and *P. aeruginosa* (Gram-negative). The minimum inhibition concentration (MIC) was first assessed from series CAZ concentration (0, 50, 100, 200, 400, 800, 1600, 3200, and 6400 μg mL^{-1}). Compared to the MIC (1600 μg mL^{-1}) for both *S. aureus* and *P. aeruginosa*, 200 μg mL^{-1} was adequate to be used in further evaluations considering its usage with NIR (Fig. S1, Supporting Information). Treatments were divided into six groups (*I*) PBS (*II*) PBS + NIR (*III*) ZnO (*IV*) ZnO + NIR (*V*) CAZ, and (*VI*) CAZ + NIR. Next, 100 μL of PBS, ZnO, and CAZ suspension were employed in the groups containing PBS, ZnO, and CAZ respectively and all groups with NIR were exposed to laser irradiation (808 nm, 2 W cm^{-2}, 7 min). The temperature of PBS, ZnO, and CAZ-treated *S. aureus* monitored with the thermal imager indicated the rapid rise in the temperature of the CAZ + NIR group (Fig. 3a and b), compared to the other groups, a demonstration of the photothermal performance of CAZ. The PBS, PBS + NIR, ZnO, and ZnO groups exhibited negligible antibacterial effects in both *S. aureus* and *P. aeruginosa* (Fig. 3c and d). On the contrary CAZ, CAZ + NIR groups demonstrated some bactericidal activity, which was obviously remarkable in the CAZ + NIR group with 97.22% and 97.13% bactericidal rates in the *S. aureus* and *P aeruginosa* respectively (Fig. 3e and f). This demonstrated that CAZ has an intrinsic bactericidal property which had an insignificant impact on the bacterial activity when solely used, but could combine with the NIR to enhance this intrinsic ability and synergistically eradicate bacteria. The intrinsic ability of the CAZ could be attributed to the Cu and Ag in the nanocomposite. Ag has a great influence on the ATP production and respiration of bacteria which could easily trigger cell death [52–54]. Also, the Cu potent antibacterial efficacy could be ascribed to the release of ions that trigger intracellular oxidative stress, genotoxicity, and subsequently cell death [55,56]. Furthermore, an investigation of the bacterial morphology with scanning electron microscopy (SEM) showed the globular and rod shapes of the *S. aureus* and *P. aeruginosa* were intact in the PBS, ZnO, ZnO + NIR, and CAZ groups (Fig. 4a and b). However, the CAZ + NIR group displayed significant wrinkling and collapse of the membrane in both *S. aureus* and *P. aeruginosa*. These confirm the results from the antibacterial assay and demonstrate that CAZ under NIR could completely eradicate bacteria via its synergistic activity.

3.4. In vitro antibiofilm activity of CAZ

Further deciphering of the *in vitro* antibacterial performance was investigated in a biofilm assay via the crystal violet calorimetric method.

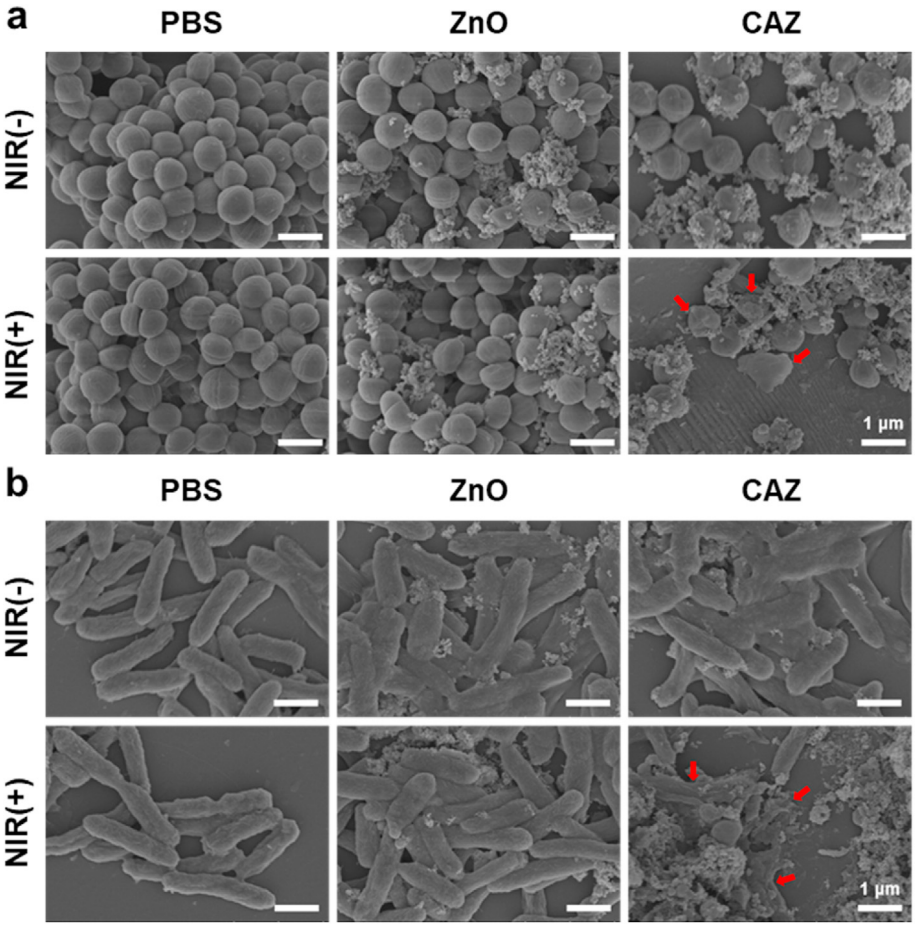

Fig. 4. Morphological changes of bacteria after incubation with CAZ NPs. SEM images of (a) *S. aureus* and (b) *P. aeruginosa* after treatment with PBS, ZnO, and CAZ NPs under 7 min of 808 nm NIR irradiation (2.0 W cm^{-2}). Control groups treated with and without NIR irradiation (scale bar: 1 μm).

Biofilms are microbial particles that aggregate via complex communication mechanisms [57,58]. As shown in (Fig. 5a), *S. aureus* biofilms in the CAZ and CAZ + NIR groups were significantly disrupted but were more obvious in the CAZ + NIR group. This suggested that the intrinsic antibacterial activity of CAZ could yield an effect after a prolonged period. On the contrary, the biofilm yield in the PBS, ZnO, and ZnO + NIR increased, which indicated negligible antibacterial or antibiofilm activity (Fig. 5b). The complete disruption of biofilm in the CAZ + NIR group showed that the antibacterial therapeutic activity of CAZ was enhanced under NIR. The live/dead staining assay was finally used to investigate the antibiofilm performance of CAZ under calcein-AM and Propidium iodide (PI) (Fig. 5c). *S. aureus* with intact membranes was stained with green fluorescence and red fluorescence represented dead bacteria stained by PI. Red fluorescence in the CAZ + NIR group was an indication of the significant bacteria disruption. Similarly, the evaluation of *S. aureus* under the live/dead staining assay confirmed the plate count assay and SEM results (Fig. S2, Supporting Information). One contributing factor to the generation of local purulent infection is the secretion of extracellular toxins by *S. aureus* [59,60]. Therefore, we investigated the inhibition rate of hemolysin. Bacteria treated under different conditions as stated in the experimental section were centrifuged at high speed, and then the supernatant was mixed with rabbit red blood cells. Following exposure to NIR, CAZ-treated *S. aureus* secreted less than 14.5% hemolysin compared to the control group (Fig. S3, Supporting Information). This result confirmed that CAZ has a good inhibitory effect on the secretion of *S. aureus* hemolysin, and can easily be employed to target *S. aureus in vivo*.

3.5. *In vivo* antibacterial performance of CAZ

Inspired by the excellent antibacterial activity *in vitro*, we evaluated the *in vivo* antibacterial activity via a bacteria-infected wound healing therapy model in Balb/c mice (8 weeks) (Fig. 6a). First, the back of the mice was shaved, disinfected with 75% ethanol, and randomly divided into 4 groups: (*I*) PBS, (*II*) PBS + NIR, (*III*) CAZ, and (*IV*) CAZ + NIR. Next, using a hole puncher small sized wounds were created on the back of mice and injected with 10 μL (10^7 CFU mL^{-1}), 20 μL of PBS, and CAZ suspensions were later injected into the wounds of the various groups, and the group with NIR exposed to (808 nm, 2 W cm^{-2}, 7 min). The temperature of the wound in the CAZ + NIR group increased remarkably reaching 55 °C within a short period (Fig. 6b). As shown in (Fig. 6c), scars began to appear in all the groups from day 2 and changed color as the day progressed. The wound size in the CAZ + NIR reduced remarkably with a recovery rate of 10.57%, compared to the PBS, PBS + NIR, and CAZ groups which showed a wound recovery rate of 41.62%, 41.38%, and 35.79% respectively (Fig. 6d). The scar in the CAZ + NIR group reduced significantly with complete disappearance after day 10. This phenomenon was observed in plated bacteria collected from the healing skin. This showed that the extent of the killing of bacteria in the wound could be attributed to the presence of intrinsic antibacterial ability from the Cu

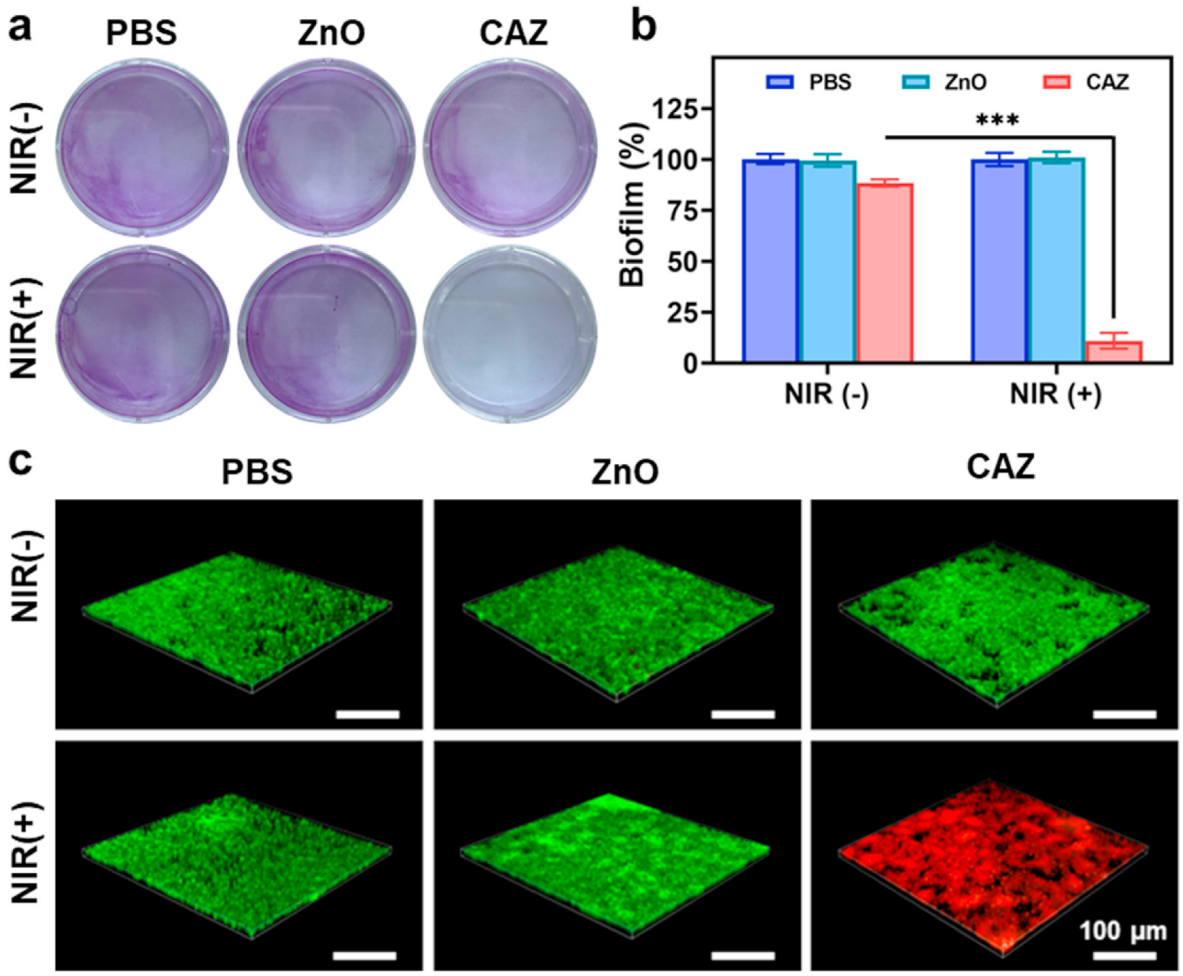

Fig. 5. Inhibition of biofilm of *S. aureus*. (a) Digital images of biofilm formation of *S. aureus* with the addition of PBS, ZnO, and CAZ under NIR (808 nm, 2.0 W cm^{-2}) for 48 h. (b) Quantitative representation of the biofilm formation under different conditions (n = 3). ***P < 0.001. (c) Confocal images of *S. aureus* biofilms stained by calcein-AM/PI under different treatments (scale bar, 100 μm).

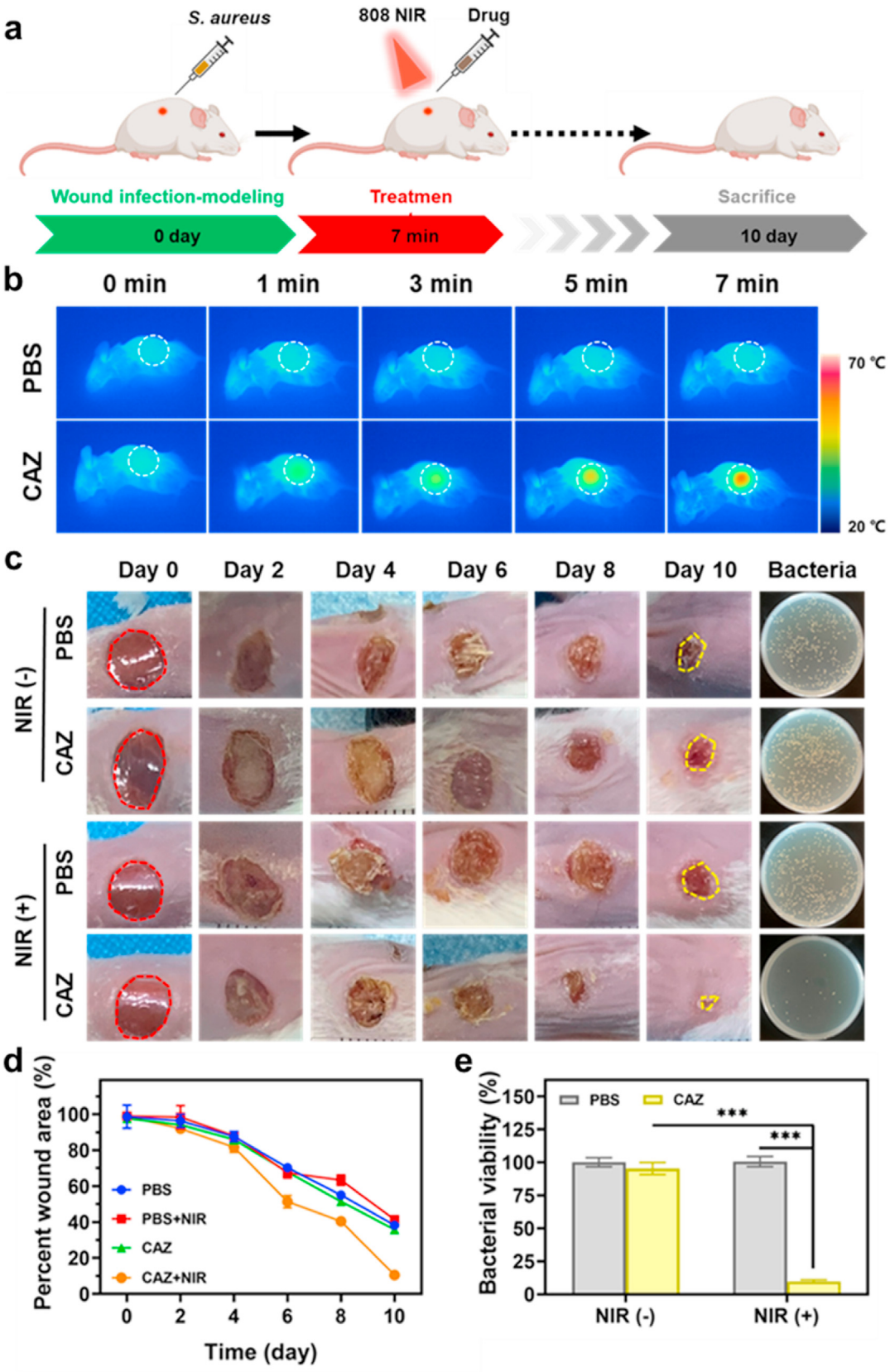

Fig. 6. Antimicrobial activity of CAZ NPs *in vivo* with a wound-infection model. (a) Schematic diagram of CAZ NPs for antibacterial therapeutic process *in vivo*. (b) Infrared thermal images of mice after different treatments under NIR irradiation (808 nm, 2.0 W cm^{-2}, 0–7 min). (c) Wound photographs of mice after different treatments at varying treatment times and photographs of bacterial colonies after 10 days of treatment. (d) Quantitative statistics of corresponding wound areas of infected mice after different treatments. (e) Quantitative statistics of bacterial colonies through standard plate counting assay (n = 3). ***P < 0.001.

and Ag, and the wound-healing effect from the Zn. Also, this indicated that CAZ singly could not have allowed for wound healing but was enhanced under the NIR. Further evaluation of the bacterial viability rate demonstrated a chunk of bacteria in the PBS, PBS + NIR, and CAZ groups with a rate of 100.12%, 100.33%, and 95.42% respectively compared to CAZ + NIR group which had 9.74% (Fig. 6e). All these demonstrated that the extent and period of bacterial infection affected wound healing and that CAZ wound healing therapeutics were enhanced under NIR.

3.6. Histopathology and biosafety evaluation

Further investigation of the treatment of the *S. aureus* infected wound was carried out by employing HE, Gram, and Masson staining (Fig. 7a). The presence of enormous neutrophils in the PBS group exhibited the remarkable gathering of inflammatory cells (yellow arrows) owing to infection. Moreover, the CAZ + NIR group displayed a significantly decreased presence of *S. aureus* based on the Gram staining (red arrows). Also, epidermal layers and collagen fibers remained intact (green arrows) in the CAZ + NIR group, an indication of perfect re-epithelization and good therapeutic efficacy of CAZ under NIR. These results demonstrated that CAZ's intrinsic therapeutic effect was enhanced under NIR. Furthermore, confirmation of the toxicity of CAZ *in vivo* was evaluated via HE staining. The main organs (heart, liver, spleen, lung, and kidney) showed no abnormality, an indication of CAZ + NIR biocompatibility, and negligible side effects (Fig. 7b). To confirm the biosafety of CAZ, an MTT assay was carried out for 48 h to assess the toxicity using L929 cells under a series of CAZ concentrations (0, 50,100, 200, 400, and 800 μg mL^{-1}) under (808 nm, 2 W cm^{-2}, 7 min). As shown in (Fig. S4, Supporting Information), almost 90% of the cells remained viable, an indication of negligible toxicity and biocompatibility of CAZ. In addition, blood chemical indexes: aminotransferase (ALT), aspartate aminotransferase (AST), alkaline phosphatase (ALP), and blood urea nitrogen (BUN) showed no remarkable blood toxicity (Fig. 8a–d), Similarly, the blood routine indexes: white blood cell (WBC), red blood cell (RBC), hemoglobin (HGB), hematocrit (HCT), mean corpuscular volume (MCV), mean corpuscular hemoglobin (MCH), platelet count (PLT) and mean platelet volume (MPV) (Fig. 8e–L), showed no obvious abnormality. All these prove the biocompatibility, hemocompatibility, and negligible toxicity of CAZ under NIR.

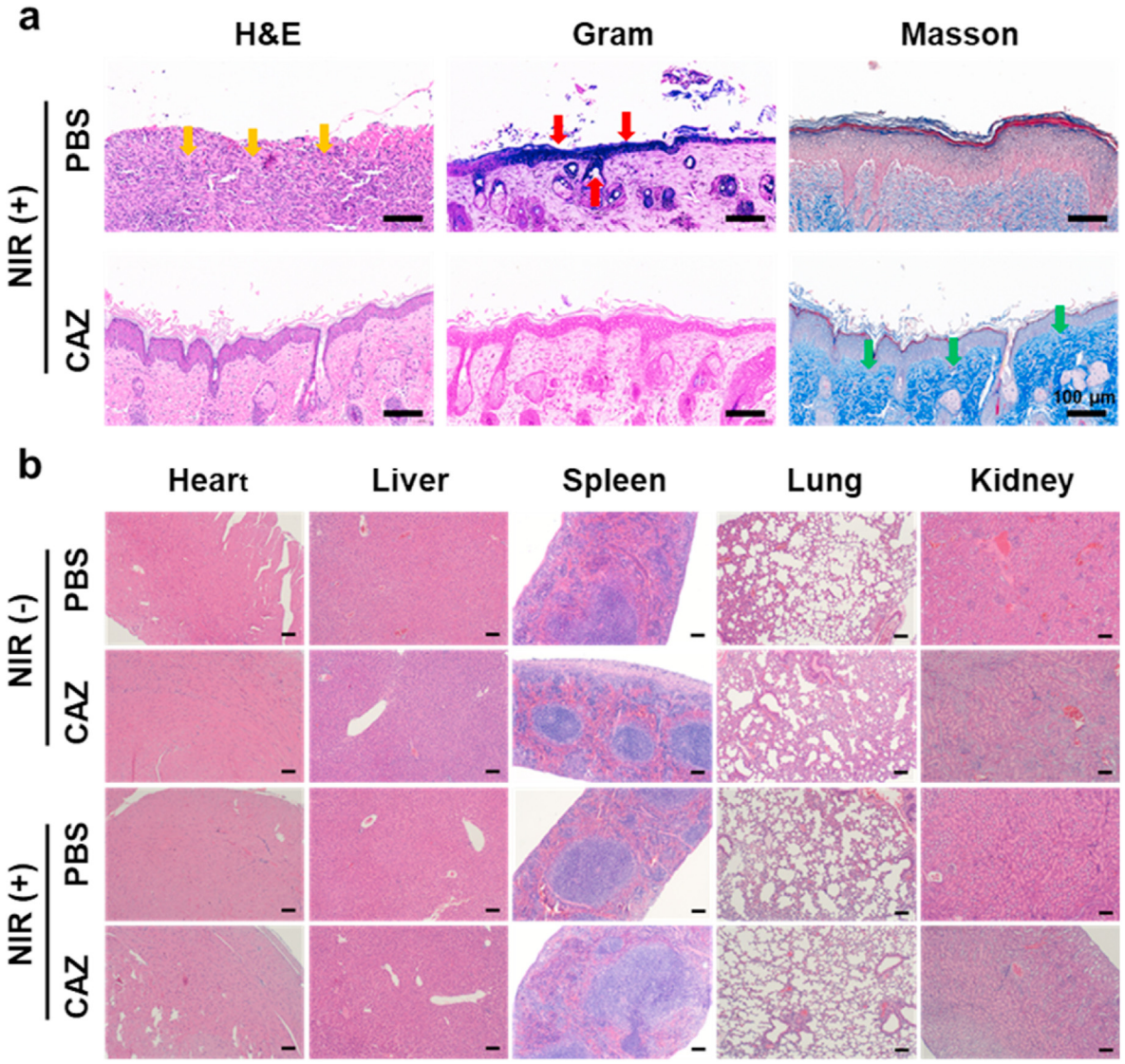

Fig. 7. (a) Histological staining results of mice-infected wounds under different treatments, including H&E, Gram stain, and Masson on day-10 (scale bar: 100 μm). (b) H&E staining images of major organs after different treatments. (Scale bar: 200 μm).

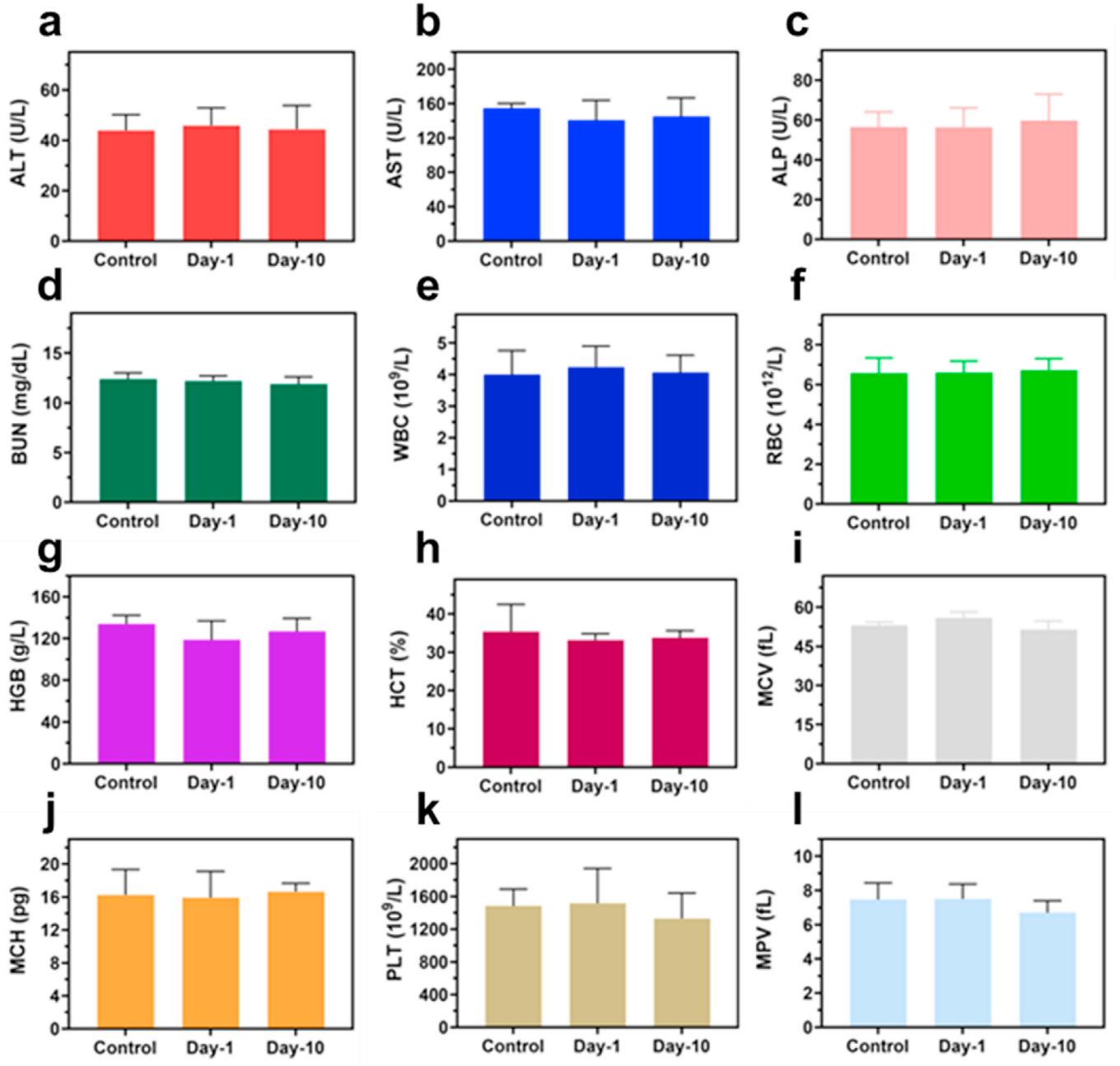

Fig. 8. Biosafety evaluations of CAZ NPs *in vivo*. Blood biochemistry examination, including (a) ALT, (b) AST, (c) ALP, and (d) BUN. Blood routine examination, including (e) WBC, (f) RBC, (g) HGB, (h) HCT, (i) MCV, (j) MCH, (k) PLT, and (l) MPV of healthy mice after subcutaneous injection under different treatment conditions at day-0, day-1, and day-10.

4. Conclusion

In summary, we successfully fabricated CuO and AgO co-modified ZnO nanocomposites, which have a good antibacterial activity that could be enhanced under NIR for a synergistic effect. Intrinsic antibacterial activity is demonstrated by a number of nanoparticles; however, their prolonged potency and effect are only demonstrated by a few nanoparticles. The study demonstrates the combination of the intrinsic antibacterial activity of both Cu and Ag with the support of the Zn component of CuO@AgO/ZnO under NIR. The *In vitro* antibacterial test suggested, that CuO@AgO/ZnO NPs could combine with NIR to synergistically induce the killing of *S. aureus* and *P. aeruginosa*. Also, CuO@AgO/ZnO NPs under NIR could disrupt *S. aureus* biofilm. More importantly, the CuO@AgO/ZnO NPs remarkably eradicated *S. aureus* in the infected wound and subsequently accelerated the healing of the wound. CuO@AgO/ZnO NPs exhibited negligible inflammatory, cellular or pathological abnormality demonstrating good biocompatibility. In all, this work provides potential prospects for the treatment of bacterial infections, promoting wound healing, and holds a promising strategy for anti-infection therapy in the biomedical field.

Credit author statement

Lisong Ye: Conceptualization, Methodology, Writing-original draft. Xiaojun He: Conceptualization, Writing-original draft, Resources. Enoch Obeng: Conceptualization, Methodology. Danyan Wang: Methodology, investigation. Dongyang Zheng: Methodology, investigation. TianXi Shen: Methodology, investigation. Jianliang Sheng: Writing-review &

editing, Supervision. Rongdang Hu: Resources, Validation, Supervision. Hui Deng: Resources, Writing-review & editing, Validation, Supervision.

Declaration of competing interest

The authors declare that they have no known competing financial interests or personal relationships that could have appeared to influence the work reported in this paper.

Data availability

Data will be made available on request.

Acknowledgments

This work was supported by the National Natural Science Foundation of China (21977081), Wenzhou Science and Technology Bureau projects (Y20190105 and Y2020594), Wenzhou Medical University (KYYW201901), Zhejiang Provincial Science and Technology Project for Public Welfare (Grant No. LGF21H140006), and Wenzhou Major Scientific and Technological Innovation Project (ZY2022020).

Appendix A. Supplementary data

Supplementary data to this article can be found online at https://doi.org/10.1016/j.mtbio.2023.100552.

References

[1] W. Zimmerli, P.D. Lew, F.A. Waldvogel, Pathogenesis of foreign body infection. Evidence for a local granulocyte defect, J. Clin. Invest. 73 (4) (1984) 1191–1200, https://doi.org/10.1172/jci111305.
[2] K.G. Barki, A. Das, S. Dixith, P.D. Ghatak, S. Mathew-Steiner, E. Schwab, S. Khanna, D.J. Wozniak, S. Roy, C.K. Sen, Electric field based dressing disrupts mixed-species bacterial biofilm infection and restores functional wound healing, Ann. Surg. 269 (4) (2019) 756–766, https://doi.org/10.1097/sla.0000000000002504.
[3] A.P. Puhto, T.M. Puhto, T.T. Niinimäki, J.I. Leppilahti, H.P. Syrjälä, Two-stage revision for prosthetic joint infection: outcome and role of reimplantation microbiology in 107 cases, J. Arthroplasty 29 (6) (2014) 1101–1104, https://doi.org/10.1016/j.arth.2013.12.027.
[4] L. Zhang, Y. Wang, J. Wang, Y. Wang, A. Chen, C. Wang, W. Mo, Y. Li, Q. Yuan, Y. Zhang, Photon-responsive antibacterial nanoplatform for synergistic photothermal-/pharmaco-therapy of skin infection, ACS Appl. Mater. Interfaces 11 (1) (2019) 300–310, https://doi.org/10.1021/acsami.8b18146.
[5] J.W. Costerton, P.S. Stewart, E.P. Greenberg, Bacterial biofilms: a common cause of persistent infections, Science 284 (5418) (1999) 1318–1322, https://doi.org/10.1126/science.284.5418.1318.
[6] F. Leone, R. Cataldo, S.S.Y. Mohamed, L. Manna, M. Banchero, S. Ronchetti, N. Mandras, V. Tullio, R. Cavalli, B. Onida, Nanostructured ZnO as multifunctional carrier for a green antibacterial drug delivery system-A feasibility study, Nanomaterials 9 (3) (2019), https://doi.org/10.3390/nano9030407.
[7] D.F. Williams, , Titanium in medicine, D.M. Brunette, P. Tengvall, M. Textor, P. Thomsen, Biomaterials, Springer, Berlin, 2001, pp. 3913–3914, https://doi.org/10.1016/S0142-9612(02)00111-4.
[8] W. Zheng, Y. Jia, Y. Zhao, J. Zhang, Y. Xie, L. Wang, X. Zhao, X. Liu, R. Tang, W. Chen, X. Jiang, Reversing bacterial resistance to gold nanoparticles by size modulation, Nano Lett. 21 (5) (2021) 1992–2000, https://doi.org/10.1021/acs.nanolett.0c04451.
[9] C. Chen, Y. Ma, S. Du, Y. Wu, P. Shen, T. Yan, X. Li, Y. Song, Z. Zha, X. Han, Controlled CRISPR-cas9 ribonucleoprotein delivery for sensitized photothermal therapy, Small 17 (33) (2021), e2101155, https://doi.org/10.1002/smll.202101155.
[10] C. Chen, S. Wang, L. Li, P. Wang, C. Chen, Z. Sun, T. Song, Bacterial magnetic nanoparticles for photothermal therapy of cancer under the guidance of MRI, Biomaterials 104 (2016) 352–360, https://doi.org/10.1016/j.biomaterials.2016.07.030.
[11] S. Bongiovanni Abel, K. Riberi, C.R. Rivarola, M. Molina, C.A. Barbero, Synthesis of a smart conductive block copolymer responsive to heat and near infrared light, Polymers 11 (11) (2019), https://doi.org/10.3390/polym11111744.
[12] H. Wang, J. Chang, M. Shi, W. Pan, N. Li, B. Tang, A dual-targeted organic photothermal agent for enhanced photothermal therapy, Angew Chem. Int. Ed. Engl. 58 (4) (2019) 1057–1061, https://doi.org/10.1002/anie.201811273.
[13] Z. Jiang, C. Zhang, X. Wang, M. Yan, Z. Ling, Y. Chen, Z. Liu, A borondifluoride-complex-based photothermal agent with an 80 % photothermal conversion efficiency for photothermal therapy in the NIR-II window, Angew Chem. Int. Ed. Engl. 60 (41) (2021) 22376–22384, https://doi.org/10.1002/anie.202107836.
[14] H.S. Jung, P. Verwilst, A. Sharma, J. Shin, J.L. Sessler, J.S. Kim, Organic molecule-based photothermal agents: an expanding photothermal therapy universe, Chem. Soc. Rev. 47 (7) (2018) 2280–2297, https://doi.org/10.1039/c7cs00522a.
[15] K.Y. Pu, A smart supramolecular phototherapeutics for specific cancer therapy, Sci. China Chem. 61 (11) (2018) 1353, https://doi.org/10.1007/s11426-018-9286-3.
[16] L. Cheng, C. Wang, L. Feng, K. Yang, Z. Liu, Functional nanomaterials for phototherapies of cancer, Chem Rev 114 (21) (2014) 10869–10939, https://doi.org/10.1021/cr400532z.
[17] A. Hatamie, A. Khan, M. Golabi, A.P. Turner, V. Beni, W.C. Mak, A. Sadollahkhani, H. Alnoor, B. Zargar, S. Bano, O. Nur, M. Willander, Zinc oxide nanostructure-modified textile and its application to biosensing, photocatalysis, and as antibacterial material, Langmuir 31 (39) (2015) 10913–10921, https://doi.org/10.1021/acs.langmuir.5b02341.
[18] Z. Lu, J. Gao, Q. He, J. Wu, D. Liang, H. Yang, R. Chen, Enhanced antibacterial and wound healing activities of microporous chitosan-Ag/ZnO composite dressing, Carbohydr. Polym. 156 (2017) 460–469, https://doi.org/10.1016/j.carbpol.2016.09.051.
[19] M.L. Ermini, V. Voliani, Antimicrobial nano-agents: the copper age, ACS Nano 15 (4) (2021) 6008–6029, https://doi.org/10.1021/acsnano.0c10756.
[20] A.B. Djurišić, Y.H. Leung, A.M. Ng, X.Y. Xu, P.K. Lee, N. Degger, R.S. Wu, Toxicity of metal oxide nanoparticles: mechanisms, characterization, and avoiding experimental artefacts, Small 11 (1) (2015) 26–44, https://doi.org/10.1002/smll.201303947.
[21] F. Fan, J. Zhang, J. Li, N. Zhang, R. Hong, X. Deng, P. Tang, D. Li, Hydrogen sensing properties of Pt-Au bimetallic nanoparticles loaded on ZnO nanorods, Sensor. Actuator. B Chem. 241 (2017) 895–903, https://doi.org/10.1016/j.snb.2016.11.025.
[22] W.L. Yu, D.F. Xu, T.Y. Peng, Enhanced photocatalytic activity of g-C3N4 for selective CO2 reduction to CH3OH via facile coupling of ZnO: a direct Z-scheme mechanism, J. Mater. Chem. 3 (39) (2015) 19936–19947, https://doi.org/10.1039/c5ta05503b.
[23] C. Yu, W. Zhou, H. Liu, Y. Liu, D.D. Dionysiou, Design and fabrication of microsphere photocatalysts for environmental purification and energy conversion, Chem. Eng. J. 287 (2016) 117–129, https://doi.org/10.1016/j.cej.2015.10.112.
[24] F. Teng, L.X. Zheng, K. Hu, H.Y. Chen, Y.M. Li, Z.M. Zhang, X.S. Fang, A surface oxide thin layer of copper nanowires enhanced the UV selective response of a ZnO film photodetector, J. Mater. Chem. C 4 (36) (2016) 8416–8421, https://doi.org/10.1039/c6tc02901a.
[25] A. Dodero, M. Alloisio, M. Castellano, S. Vicini, Multilayer alginate-polycaprolactone electrospun membranes as skin wound patches with drug delivery abilities, ACS Appl. Mater. Interfaces 12 (28) (2020) 31162–31171, https://doi.org/10.1021/acsami.0c07352.
[26] A.S. Soubhagya, A. Moorthi, M. Prabaharan, Preparation and characterization of chitosan/pectin/ZnO porous films for wound healing, Int. J. Biol. Macromol. 157 (2020) 135–145, https://doi.org/10.1016/j.ijbiomac.2020.04.156.
[27] A. Hui, F. Yang, R. Yan, Y. Kang, A. Wang, Palygorskite-based organic-inorganic hybrid nanocomposite for enhanced antibacterial activities, Nanomaterials 11 (12) (2021), https://doi.org/10.3390/nano11123230.
[28] L. Ai, Y. Wang, G. Tao, P. Zhao, A. Umar, P. Wang, H. He, Polydopamine-based surface modification of ZnO nanoparticles on sericin/polyvinyl alcohol composite film for antibacterial application, Molecules 24 (3) (2019), https://doi.org/10.3390/molecules24030503.
[29] B. Zhang, L. Cui, K. Zhang, Dosage- and time-dependent antibacterial effect of zinc oxide nanoparticles determined by a highly uniform SERS negating undesired spectral variation, Anal. Bioanal. Chem. 408 (14) (2016) 3853–3865, https://doi.org/10.1007/s00216-016-9478-z.
[30] T. Bruna, F. Maldonado-Bravo, P. Jara, N. Caro, Silver nanoparticles and their antibacterial applications, Int. J. Mol. Sci. 22 (13) (2021), https://doi.org/10.3390/ijms22137202.
[31] M. Azizi-Lalabadi, F. Garavand, S.M. Jafari, Incorporation of silver nanoparticles into active antimicrobial nanocomposites: release behavior, analyzing techniques, applications and safety issues, Adv. Colloid Interface Sci. 293 (2021), 102440, https://doi.org/10.1016/j.cis.2021.102440.
[32] L. Zhang, S. Gao, F. Zhang, K. Yang, Q. Ma, L. Zhu, Activatable hyaluronic acid nanoparticle as a theranostic agent for optical/photoacoustic image-guided photothermal therapy, ACS Nano 8 (12) (2014) 12250–12258, https://doi.org/10.1021/nn506130t.
[33] J. Liu, R.H. Hurt, Ion release kinetics and particle persistence in aqueous nano-silver colloids, Environ. Sci. Technol. 44 (6) (2010) 2169–2175, https://doi.org/10.1021/es9035557.
[34] E. Obeng, J. Feng, D. Wang, D. Zheng, B. Xiang, J. Shen, Multifunctional phototheranostic agent ZnO@Ag for anti-infection through photothermal/photodynamic therapy, Front. Chem. 10 (2022), 1054739, https://doi.org/10.3389/fchem.2022.1054739.
[35] W. Shao, X. Liu, H. Min, G. Dong, Q. Feng, S. Zuo, Preparation, characterization, and antibacterial activity of silver nanoparticle-decorated graphene oxide nanocomposite, ACS Appl. Mater. Interfaces 7 (12) (2015) 6966–6973, https://doi.org/10.1021/acsami.5b00937.
[36] Y. Qiao, Y. Ping, H. Zhang, B. Zhou, F. Liu, Y. Yu, T. Xie, W. Li, D. Zhong, Y. Zhang, K. Yao, H.A. Santos, M. Zhou, Laser-activatable CuS nanodots to treat multidrug-resistant bacteria and release copper ion to accelerate healing of infected chronic nonhealing wounds, ACS Appl. Mater. Interfaces 11 (4) (2019) 3809–3822, https://doi.org/10.1021/acsami.8b21766.
[37] M. Li, X. Liu, L. Tan, Z. Cui, X. Yang, Z. Li, Y. Zheng, K.W.K. Yeung, P.K. Chu, S. Wu, Noninvasive rapid bacteria-killing and acceleration of wound healing through

photothermal/photodynamic/copper ion synergistic action of a hybrid hydrogel, Biomater. Sci. 6 (8) (2018) 2110–2121, https://doi.org/10.1039/c8bm00499d.
[38] A. Singh, A. Ahmed, K.N. Prasad, S. Khanduja, S.K. Singh, J.K. Srivastava, N.S. Gajbhiye, Antibiofilm and membrane-damaging potential of cuprous oxide nanoparticles against Staphylococcus aureus with reduced susceptibility to vancomycin, Antimicrob. Agents Chemother. 59 (11) (2015) 6882–6890, https://doi.org/10.1128/aac.01440-15.
[39] S. Zhang, J. Lu, Y. Wang, W. Verstraete, Z. Yuan, J. Guo, Insights of metallic nanoparticles and ions in accelerating the bacterial uptake of antibiotic resistance genes, J. Hazard Mater. 421 (2022), 126728, https://doi.org/10.1016/j.jhazmat.2021.126728.
[40] Y.C. Ko, H.Y. Fang, D.H. Chen, Fabrication of Ag/ZnO/reduced graphene oxide nanocomposite for SERS detection and multiway killing of bacteria, J. Alloys Compd. 695 (2017) 1145–1153, https://doi.org/10.1016/j.jallcom.2016.10.241.
[41] Y. Cao, H.A. Dhahad, M.A. El-Shorbagy, H.Q. Alijani, M. Zakeri, A. Heydari, E. Bahonar, M. Slouf, M. Khatami, M. Naderifar, S. Iravani, S. Khatami, F.F. Dehkordi, Green synthesis of bimetallic ZnO-CuO nanoparticles and their cytotoxicity properties, Sci. Rep. 11 (1) (2021), 23479, https://doi.org/10.1038/s41598-021-02937-1.
[42] M. Nie, H. Sun, H.L. Cai, Z.H. Xue, C. Yang, Q. Li, L.Z. Qin, M.Y. Wu, Study on electrocatalytic property of ZnO and Ag/ZnO, Mater. Lett. 271 (2020), https://doi.org/10.1016/j.matlet.2020.127785.
[43] D. Hu, H. Li, B. Wang, Z. Ye, W. Lei, F. Jia, Q. Jin, K.F. Ren, J. Ji, Surface-adaptive gold nanoparticles with effective adherence and enhanced photothermal ablation of methicillin-resistant Staphylococcus aureus biofilm, ACS Nano 11 (9) (2017) 9330–9339, https://doi.org/10.1021/acsnano.7b04731.
[44] C. Han, Z. Li, W.J. Li, S.L. Chou, S.X. Dou, Controlled synthesis of copper telluride nanostructures for long-cycling anodes in lithium ion batteries, J. Mater. Chem. 2 (30) (2014) 11683–11690, https://doi.org/10.1039/c4ta01579g.
[45] M.S. Usman, N.A. Ibrahim, K. Shameli, N. Zainuddin, W.M. Yunus, Copper nanoparticles mediated by chitosan: synthesis and characterization via chemical methods, Molecules 17 (12) (2012) 14928–14936, https://doi.org/10.3390/molecules171214928.
[46] A.N. Kadam, D.P. Bhopate, V.V. Kondalkar, S.M. Majhi, C.D. Bathula, A.V. Tran, S.W. Lee, Facile synthesis of Ag-ZnO core-shell nanostructures with enhanced photocatalytic activity, J. Ind. Eng. Chem. 61 (2018) 78–86, https://doi.org/10.1016/j.jiec.2017.12.003.
[47] Y. Chen, W.H. Tse, L. Chen, J. Zhang, Ag nanoparticles-decorated ZnO nanorod array on a mechanical flexible substrate with enhanced optical and antimicrobial properties, Nanoscale Res. Lett. 10 (2015) 106, https://doi.org/10.1186/s11671-014-0712-3.
[48] J. Halim, S. Kota, M.R. Lukatskaya, M. Naguib, M.-Q. Zhao, E.J. Moon, J. Pitock, J. Nanda, S.J. May, Y. Gogotsi, M.W. Barsoum, Synthesis and characterization of 2D molybdenum carbide (MXene), Adv. Funct. Mater. 26 (18) (2016) 3118–3127, https://doi.org/10.1002/adfm.201505328.
[49] J. Zeng, D. Goldfeld, Y. Xia, A plasmon-assisted optofluidic (PAOF) system for measuring the photothermal conversion efficiencies of gold nanostructures and controlling an electrical switch, Angew Chem. Int. Ed. Engl. 52 (15) (2013) 4169–4173, https://doi.org/10.1002/anie.201210359.
[50] M. Manikandan, N. Hasan, H.F. Wu, Platinum nanoparticles for the photothermal treatment of Neuro 2A cancer cells, Biomaterials 34 (23) (2013) 5833–5842, https://doi.org/10.1016/j.biomaterials.2013.03.077.
[51] P. Liu, Y. Wang, L. An, Q. Tian, J. Lin, S. Yang, Ultrasmall WO(3- x)@γ-poly-l-glutamic acid nanoparticles as a photoacoustic imaging and effective photothermal-enhanced chemodynamic therapy agent for cancer, ACS Appl. Mater. Interfaces 10 (45) (2018) 38833–38844, https://doi.org/10.1021/acsami.8b15678.
[52] M. Hassan, M. Kjos, I.F. Nes, D.B. Diep, F. Lotfipour, Natural antimicrobial peptides from bacteria: characteristics and potential applications to fight against antibiotic resistance, J. Appl. Microbiol. 113 (4) (2012) 723–736, https://doi.org/10.1111/j.1365-2672.2012.05338.x.
[53] Y. Tian, J. Qi, W. Zhang, Q. Cai, X. Jiang, Facile, one-pot synthesis, and antibacterial activity of mesoporous silica nanoparticles decorated with well-dispersed silver nanoparticles, ACS Appl. Mater. Interfaces 6 (15) (2014) 12038–12045, https://doi.org/10.1021/am5026424.
[54] K. Rajavel, R. Gomathi, S. Manian, R.T. Rajendra Kumar, In vitro bacterial cytotoxicity of CNTs: reactive oxygen species mediate cell damage edges over direct physical puncturing, Langmuir 30 (2) (2014) 592–601, https://doi.org/10.1021/la403332b.
[55] G. Grass, C. Rensing, M. Solioz, Metallic copper as an antimicrobial surface, Appl. Environ. Microbiol. 77 (5) (2011) 1541–1547, https://doi.org/10.1128/aem.02766-10.
[56] M. Vincent, R.E. Duval, P. Hartemann, M. Engels-Deutsch, Contact killing and antimicrobial properties of copper, J. Appl. Microbiol. 124 (5) (2018) 1032–1046, https://doi.org/10.1111/jam.13681.
[57] D. Davies, Understanding biofilm resistance to antibacterial agents, Nat. Rev. Drug Discov. 2 (2) (2003) 114–122, https://doi.org/10.1038/nrd1008.
[58] Y. Liu, B. Xu, M. Lu, S. Li, J. Guo, F. Chen, X. Xiong, Z. Yin, H. Liu, D. Zhou, Ultrasmall Fe-doped carbon dots nanozymes for photoenhanced antibacterial therapy and wound healing, Bioact. Mater. 12 (2022) 246–256, https://doi.org/10.1016/j.bioactmat.2021.10.023.
[59] L. Thomer, O. Schneewind, D. Missiakas, Pathogenesis of Staphylococcus aureus bloodstream infections, Annu. Rev. Pathol. 11 (2016) 343–364, https://doi.org/10.1146/annurev-pathol-012615-044351.
[60] M. Laabei, A.C. Uhlemann, F.D. Lowy, E.D. Austin, M. Yokoyama, K. Ouadi, E. Feil, H.A. Thorpe, B. Williams, M. Perkins, S.J. Peacock, S.R. Clarke, J. Dordel, M. Holden, A.A. Votintseva, R. Bowden, D.W. Crook, B.C. Young, D.J. Wilson, M. Recker, R.C. Massey, Evolutionary trade-offs underlie the multi-faceted virulence of Staphylococcus aureus, PLoS Biol. 13 (9) (2015), e1002229, https://doi.org/10.1371/journal.pbio.1002229.